Nonlinear resonant behavior of the dispersive readout scheme for a superconducting flux qubit

Janice C. Lee,[1] William D. Oliver,[2] Karl K. Berggren,[2, *] and T. P. Orlando[1]

[1]*Department of Electrical Engineering and Computer Science,*
Massachusetts Institute of Technology, Cambridge, Massachusetts 02139, USA
[2]*MIT Lincoln Laboratory, 44 Wood Street, Lexington, Massachusetts 02420, USA*
(Dated: February 6, 2008)

A nonlinear resonant circuit comprising a SQUID magnetometer and a parallel capacitor is studied as a readout scheme for a persistent-current (PC) qubit. The flux state of the qubit is detected as a change in the Josephson inductance of the SQUID magnetometer, which in turn mediates a shift in the resonance frequency of the readout circuit. The nonlinearity and resulting hysteresis in the resonant behavior are characterized as a function of the power of both the input drive and the associated resonance peak response. Numerical simulations based on a phenomenological circuit model are presented which display the features of the observed nonlinearity.

PACS numbers:

I. INTRODUCTION

Superconducting Josephson junction circuits are promising candidates for realizing a quantum computer. These solid-state qubits can be fabricated using standard integrated-circuit techniques, where there is the possibility to incorporate the control and readout circuitry on-chip, providing a manageable option for scaling up to a larger number of qubits. Quantum-coherent phenomena [1] have been studied utilizing the quantum states [2] of single-qubit circuits and cavities, including superpositions of distinct macroscopic states [3, 4], time-dependent Rabi oscillations [5, 6, 7, 8, 9, 10, 11], cavity quantum-electrodynamics [12, 13, 14] and Mach-Zehnder-type interferometry [15, 16, 17]. Coherent oscillations [18], spectroscopic evidence for entanglement [19], and a prototypical gate operation [20] have also been demonstrated in superconducting coupled-qubits. However, to further increase the coherence times of these qubits for manipulation of their quantum states, one must find ways to reduce the amount of noise intrinsic to the qubit, as well as noise introduced by the readout process itself. In particular, several previous readout methods have relied on the switching of a Josephson circuit from a zero-voltage to a finite-voltage state. This switching generates quasiparticles, and thus such readout approach is limited by the subsequent decoherence. More recently dispersive readout schemes have been developed such that the qubit is coupled to a resonator, and the state of the qubit is detected as a shift in the resonance frequency of the resonator. As a result, the readout process requires only lower input biases and hence minimizes the generation of quasiparticles. Furthermore, the resonator also acts as a narrow-band filter which shields the qubit from broad-band noise. Dispersive readout has been implemented for

the persistent current qubit [21, 22], for the charge qubit [23], and for the hybrid qubit where the readout was operated in the nonlinear regime for its use as a bifurcation amplifier [24].
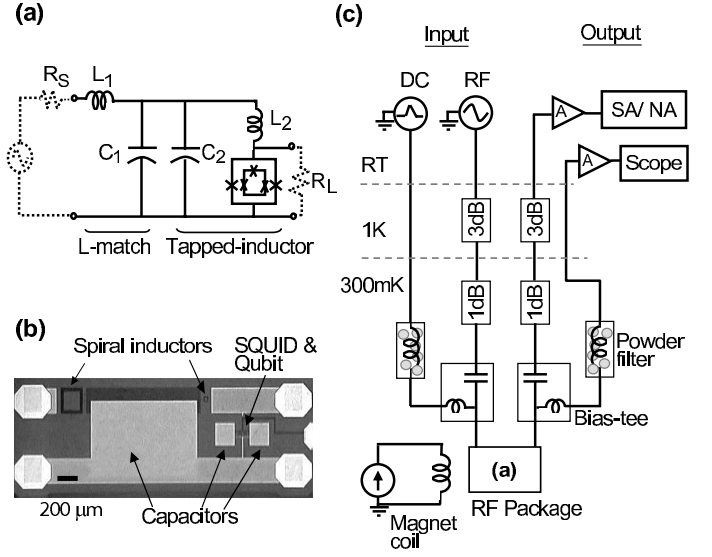

FIG. 1: Experimental setup: (a) Circuit schematic of the resonant readout circuit. The designed component values were $L_1 = 69\,\text{nH}$, $L_2 = 0.78\,\text{nH}$, $C_1 = 1.4\,\text{pF}$, and $C_2 = 100\,\text{pF}$. The SQUID inductance L_J was approximated to be $0.2\,\text{nH}$ for the circuit design. (b) Optical micrograph of the actual device. (c) Electronic setup at different temperature stages of the ^{3}He cryostat.

This paper focuses on characterizing the nonlinear resonant behavior of the dispersive readout scheme developed for a persistent current qubit. The readout element is a SQUID magnetometer, which is operated as a nonlinear, flux-sensitive inductor incorporated in an L-C resonator. The qubit is coupled to the SQUID inductor, and the flux state of the qubit is detected as a shift in the

---

*Present address: EECS Department, MIT

resonance frequency of the resonator by means of magnitude and/or phase measurements. Our approach differs from other resonant-type experiments in two main ways. First, our qubit and readout circuit were fabricated on the same chip from niobium, whereas the implementations in [21]-[24] were aluminum-based. Second, we were able to achieve a high quality factor for the resonator by incorporating an RF transformation network on-chip using the planarized niobium process. We observed resonant behavior due to the nonlinear Josephson inductance of the SQUID, given the high quality factor of the resonance [25, 26]. The frequency spectra of the readout circuit were characterized in both the linear and nonlinear regimes. Biasing the readout circuit in the nonlinear regime potentially provides additional sensitivity for distinguishing the qubit states [24].

The persistent current (PC) qubit used in this study is a superconducting loop interrupted by three Josephson junctions, two of which have the same critical current while the third junction has a critical current reduced by a factor α [27, 28]. When the external magnetic flux threading the qubit loop is biased near half a flux quantum, the two lowest energy states correspond to oppositely circulating persistent currents in the qubit loop. The induced flux of the persistent current (and hence the state of the qubit) is detected by a SQUID magnetometer which surrounds the qubit.

In the resonant readout scheme, the SQUID magnetometer is operated using the property that the Josephson inductance of the SQUID is a nonlinear function of both the current bias I_{sq} and the flux bias Φ_{ext}. In our experiments, the SQUID current bias comprises solely an AC component, whereas the flux bias $\Phi_{ext} = \Phi_{dc} + \Phi_{ac}$ has both a DC component corresponding to the external bias, and an AC component corresponding to the induced flux that is mutually coupled to the SQUID. To demonstrate the general principles underlying the operation, consider the limiting case where the SQUID has negligible loop inductance and symmetric junctions each with critical current I_{co}. In this limit, the SQUID behaves like an equivalent single junction with an effective critical current given by $I_c(\Phi_{ext}) = 2I_{co}|\cos(\pi\Phi_{ext}/\Phi_o)|$, and an effective phase given by $\varphi_p = \sin^{-1}(I_{sq}/I_c(\Phi_{ext}))$. By defining the Josephson inductance according to $V_{sq} = d\left[L_J I_{sq}\right]/dt$, where V_{sq} is the voltage across the SQUID, we obtain the inductance to be

$$L_J(I_{sq}, \Phi_{ext}) = \frac{\Phi_o}{2\pi I_c(\Phi_{ext})} \frac{\varphi_p}{\sin \varphi_p} \ . \tag{1}$$

In the linear regime where the current and flux biases are small, one can approximate the SQUID by a linear inductor given by

$$L_{Jo} = \frac{\Phi_o}{4\pi I_{co}} \ . \tag{2}$$

The inductance for small AC drives can be approximated quasi-statically by the inductance at the DC operating points for the current and flux biases. To demonstrate

the separate effects due to the current and the flux, we first set Φ_{ext} to zero and reduce Eqn. 1 to

$$L_J(I_{sq}, 0) = 2L_{Jo}\frac{\varphi_p}{\sin \varphi_p} \ , \tag{3}$$

where $\varphi_p = \sin^{-1}(I_{sq}/2I_{co})$. Thus, the inductance increases with the size of the driving DC current bias. Likewise, when I_{sq} in Eqn. 1 is set to zero,

$$L_J(0, \Phi_{ext}) = \frac{L_{Jo}}{\left|\cos\left(\frac{\pi\Phi_{ext}}{\Phi_o}\right)\right|} \tag{4}$$

which has a periodic dependence on the DC flux bias with periodicity given by Φ_o. Starting from a bias of $\Phi_{dc} = 0$, the inductance increases with flux, and starting from a bias of $\Phi_{dc} = 0.5\,\Phi_o$, the inductance decreases with flux.

The general trend of an AC bias can be conceptualized as averaging the inductance about the DC bias point over the range of the AC bias. Hence, near $\Phi_{dc} = 0$ both the AC driving current and the AC flux increase the effective inductance as the AC drives increase. In contrast, near $\Phi_{dc} = 0.5\,\Phi_o$ an increasing AC flux bias tends to decrease the effective inductance and an increasing AC current bias tends to have the opposite effect. Therefore,the current and flux act in concert at $\Phi_{dc} = 0$; whereas, they compete at $\Phi_{dc} = 0.5\,\Phi_o$. From our experiments and numerical simulations [29], we have found in our readout circuit that the AC flux dominates at $\Phi_{dc} = 0.5\,\Phi_o$. Consequently, this paper will focus on the effects due to flux, thereby allowing us to develop a phenomenological model that qualitatively matches the experimental observations.

Fig. 1a shows the circuit schematic of the resonant readout circuit. The PC qubit is mutually coupled to the SQUID inductor L_J. The resonating loop comprises L_J, L_2, and the parallel combination of C_1 and C_2. To raise the quality factor of the resonance for higher readout sensitivity, a tapped-inductor transformer formed by L_2 and L_J is used to step up the effective output resistance at the resonance frequency. On the input side, L_1 and C_1 form an L-match network which matches the input resistance to the transformed output resistance [30]. R_s and R_L represent the $50\,\Omega$ source and load impedances from the RF electronics, and no resistors were fabricated on-chip. The junctions of the SQUID are each shunted by a 5 pF capacitor (not shown). The device was fabricated using the planarized niobium trilayer process at MIT Lincoln Laboratory [31]. A device micrograph is shown in Fig. 1b. The Josephson critical current density was estimated to be $1.2\,\mu\text{A}/\mu\text{m}^2$ from the process test data. The designed junction dimensions were $1.0\,\mu\text{m}$ and $0.9\,\mu\text{m}$ for the qubit, and $1.5\,\mu\text{m}$ for the SQUID. Due to process bias, the effective electrical junction dimensions are expected to be smaller. We measured the effective size of the SQUID junctions to be approximately $1.3\,\mu\text{m}$, a reduction of $0.2\,\mu\text{m}$ from their drawn dimension. The effective qubit junction sizes were not measured directly, but were estimated to have a reduction of approximately

0.35 μm, as determined by measuring similarly drawn 1.0 μm process-test junctions nearby. The area ratio of the SQUID to the qubit loop was designed to be 1.3, with mutual coupling estimated to be 30 pH. The inductors were realized by square spirals with a linewidth and spacing of 1 μm, while the capacitors comprised Nb electrodes with a dielectric consisting of 50 nm of Nb_2O_5 and 200 nm of SiO_2.

Our measurements were taken in a ^{3}He cryostat at 300 mK. The measurement setup is shown in Fig. 1c. The DC lines were used to characterize the junction properties, while the RF lines were used for the resonant readout. The external DC flux bias for the qubit was provided by a superconducting coil wrapped around the sample housing. The signal from the resonant circuit was amplified at room temperature. We measured the transmission characteristics of the readout circuit with a spectrum analyzer equipped with a tracking generator, or with a network analyzer when the phase information was needed. We used a resolution bandwidth (RBW) of 3 kHz, and averaged each spectrum 100 times.

II. QUBIT READOUT AND EFFECT OF INPUT BIAS ON READOUT CIRCUIT

The resonance frequency of the readout circuit was measured to be near 419 MHz, with a quality factor estimated to be on the order of 1000. Fig. 2a shows the results when an external flux bias Φ_{dc} was applied through the sample. At a given Φ_{dc}, we measured both the resonance frequency and the peak power of the resonance spectrum. The resonance frequency of the readout circuit, in the linear regime where all the AC biases are small, is related to the effective inductance L_J and capacitance C by

$$f_o(\Phi_{dc}) = \frac{1}{2\pi\sqrt{L_J(\Phi_{dc})C}} \; . \qquad (5)$$

A periodic modulation of the resonance frequency of the readout circuit was observed and is interpreted as being caused by the periodic modulation of the Josephson inductance of the SQUID. At every 1.3 times the SQUID modulation period, a shift in the resonance frequency, corresponding to about 2 pH (1%) change in Josephson inductance, was observed. These shifts, referred to as qubit steps, occur as the flux in the qubit Φ_q is swept past $\Phi_q = 0.5\,\Phi_o$, as it is more energetically favorable for the qubit to change from one circulating current state to the other in order to remain in the ground state. The periodicity of the qubit steps (corresponding to a flux quantum for the qubit) and the periodicity of the SQUID lobes (corresponding to a flux quantum for the SQUID) are related by the ratio of their loop areas, which was defined by the fabrication parameters. In addition, we observed a dip in the resonance-peak power (not shown), which corresponds to a broadening of the resonance near the qubit step region [32]. The parabolic-like background

observed in the frequency modulation curve was due to undesired heating from the magnet current in the DC (soft-coax) lines. The heating causes an increase in the resonance frequency, and is more significant at high magnet current biases. The heating effect was eliminated for faster scans and when the sample was later tested in a dilution refrigerator using superconducting magnet leads.
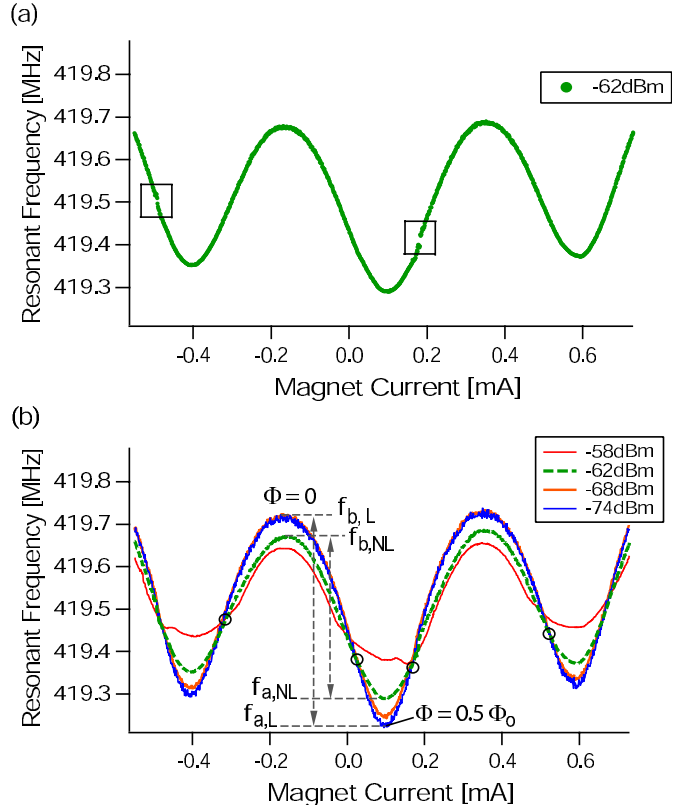
(a)

(b)

FIG. 2: (Color online)(a) Modulation of the resonance frequency with external DC flux bias. Qubit steps are observed at 0.18 mA and -0.495 mA. (b) Modulation of the resonance frequency for various input power. Amount of modulation is reduced in the nonlinear regime ($f_{b,NL} - f_{a,NL}$) compared to the linear regime ($f_{b,L} - f_{a,L}$). The circular markers represent the inflection points where $d^2 f_o/d\Phi^2 = 0$.

Fig. 2b shows that as the level of input bias increases, the amount by which the frequency is modulated over a flux quantum decreases. This will be shown in the next section to be a direct consequence of the shape of the resonance spectrum as it becomes increasingly nonlinear with higher input power.

III. NONLINEAR RESONANT BEHAVIOR OF READOUT CIRCUIT

The resonant readout circuit can experimentally distinguish the difference in the flux produced by the circulating current states of the qubit. Given that the efficacy of the readout scheme depends on the nonlinear response

of the readout circuit, we now characterize the resonant behavior of the readout circuit as a function of the DC flux bias for higher AC drives.

Fig. 3 shows the evolution of the magnitude and phase spectra with increasing input power for external flux biases of $\Phi_{dc} = 0$, $0.3\,\Phi_o$ and $0.5\,\Phi_o$. In the case when $\Phi_{dc} = 0$, the magnitude and phase spectra evolve from a symmetric shape to being asymmetric with a lower resonance frequency as the power of the drive is increased. The lower resonance frequency indicates that the effective Josephson inductance over an oscillating period is higher. For higher levels of the input power, the magnitude spectrum exhibits a discontinuity near the resonance frequency, where the system jumps from the lower branch to the higher branch. The phase spectrum also exhibits a discontinuity similar to the magnitude spectrum. For $\Phi_{dc} = 0.5\,\Phi_o$, the asymmetry is opposite to that of $\Phi_{dc} = 0$; the resonance frequency increases with higher power, indicating that the overall effective inductance is decreasing with increasing power of the drive. An intermediate behavior is captured at $\Phi_{dc} = 0.3\,\Phi_o$. As the input power increases, the nonlinear magnitude spectrum first bends towards the lower frequency side, then gradually evolves into a characteristic shape with two discontinuities near the resonance frequency, once when the magnitude is increasing and once when the magnitude is decreasing. Similarly, the phase spectrum also shows two discontinuities at the same frequency locations, with a partial phase drop at each discontinuity.
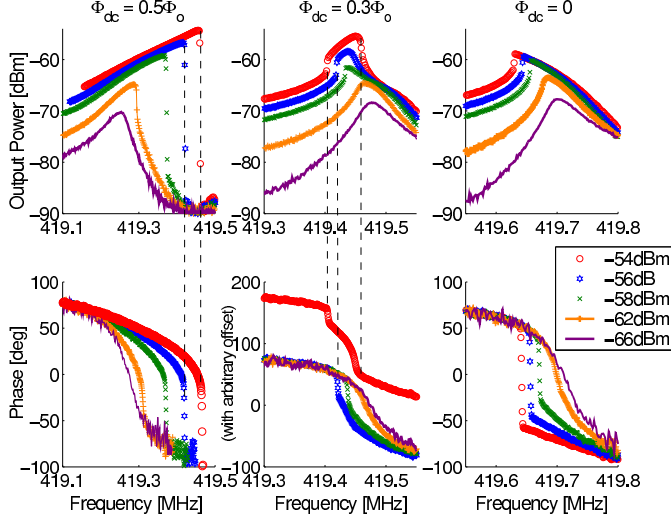

FIG. 3: Evolution of the magnitude and phase spectra of the readout circuit from the linear to the nonlinear regime with increasing input power. Data are shown for flux biases at $\Phi_{dc} = 0$, $0.3\,\Phi_o$ and $0.5\,\Phi_o$. The nonlinear spectrum evolves from having a lower resonance frequency at $\Phi = 0$ to having a higher resonance frequency at $\Phi = 0.5\,\Phi_o$. A self-resonance (due to parasitic couplings) was observed near the resonance frequency of the spectrum. The phase spectrum at -54 dBm for $\Phi = 0.3\,\Phi_o$ was arbitrarily shifted for display purpose.

The shapes of these curves are similar to the response

of driven, weakly nonlinear systems which exhibit an instability region indicating multiple solutions and hysteresis [33, 34]. Two such curves are shown in Fig. 4a and b. In particular, we model our system as a nonlinear circuit which results from a current-driven LRC resonant circuit with a nonlinear inductor L. In this case the flux in the inductor Φ satisfies

$$I\sin\omega_s t = C\frac{d^2\Phi}{dt^2} + \frac{1}{R}\frac{d\Phi}{dt} + h(\Phi, d\Phi/dt)\,, \qquad (6)$$

where the function $h(\Phi, d\Phi/dt)$ models the nonlinearity of the inductor. For example, when $h = \Phi/L_o$ then the system is a simple LRC resonant circuit with a linear inductor L_o. When $h \sim \sin\Phi$ the nonlinear equation is analogous to a driven pendulum system whose response is similar to Fig. 4b [33, 37]. Another example is the Duffing Equation where $h \sim \Phi - c\Phi^3$, whose response is like Fig. 4a for negative c and like Fig. 4b for positive c [33, 34]. In section V we will use a functional form for the effective inductance which incorporates both the needed dependence on applied DC flux and the resonance-frequency dependence observed for small drives. In fact, given that Fig. 2 shows that the resonance frequency is periodic in the applied DC flux, then the effective inductance that needs to be captured in the form of h must also follow this same periodicity.
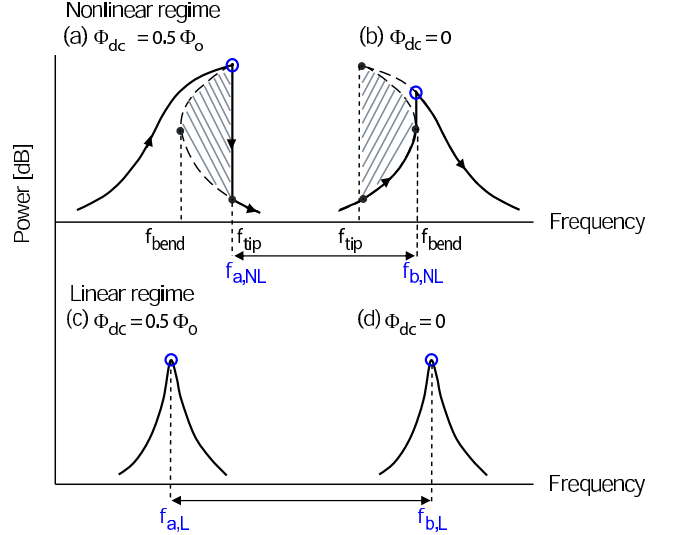

FIG. 4: Illustration of the resonance spectra in the nonlinear regime (a and b) and the linear regime (c and d) for $\Phi = 0.5\,\Phi_o$ and $\Phi = 0$ respectively. The shaded region of the nonlinear spectrum marks the region over which multiple solutions occur. The solid line traces the actual spectrum observed experimentally with a forward frequency sweep, and the circular marker corresponds to the peak frequency that was being measured. The bending of the nonlinear spectra to opposite sides accounts for the reduced separation of resonance frequencies $(f_{b,NL} - f_{a,NL})$ compared to the linear case $(f_{b,L} - f_{a,L})$, as was observed in Fig. 2b.

We now use the illustration in Fig. 4 to explain some of the general features of the data in Fig. 2 and to motivate

the subsequent analysis. In Fig. 4, the shape of the resonance spectra are shown for both the linear and nonlinear regimes for $\Phi_{dc} = 0$ and $0.5\,\Phi_o$, with the resonance frequency at $\Phi_{dc} = 0.5\,\Phi_o$ lower than at $\Phi_{dc} = 0$ given the flux-dependence of the effective inductance. The shaded region of the nonlinear spectrum corresponds to the region $f \in [f_{tip}, f_{bend}]$ over which multiple solutions occur (two of which are stable and one of which is unstable) [35]. The solid line traces the actual spectrum observed experimentally with a forward frequency sweep, and the circular marker corresponds to the peak frequency that was being measured.

We have seen from Fig. 2b that as the level of input power increases, the amount by which the frequency is modulated over a flux quantum decreases. This is a direct consequence of the shape of the resonance spectrum as the system response becomes increasingly nonlinear. As illustrated in Figs. 4c and d, the resonance spectra at $\Phi = 0$ and $0.5\,\Phi_o$ have resonance frequencies that are maximally separated $(f_{b,L} - f_{a,L})$ when the input bias is low, and therefore when the resonance spectra are nearly those of a linear response. As the input current bias increases, the resonance spectrum evolves from the symmetric Lorentzian shape to an asymmetric shape. This is shown in Figs. 4a and b. The fact that the nonlinear spectra bend to opposite sides at $\Phi = 0$ and $0.5\,\Phi_o$ accounts for a reduced amount of modulation in resonance frequency $(f_{b,NL} - f_{a,NL})$ compared to the linear case. It was also observed in Fig. 2b that the frequency modulation curves for different input power meet periodically at the inflection points, where the second derivative $d^2 f_o/d\Phi^2$ equals zero. In fact, the asymmetry of the spectrum changes sign near the inflection points.

To further quantify the amount of bending in the nonlinear spectrum, we introduce a parameter δf which is a normalized shift of the resonance frequency f_n of the nonlinear spectrum relative to the linear spectrum f_o:

$$\delta f = \frac{f_n - f_o}{f_o} \, . \tag{7}$$

Experimentally, f_o was determined as the resonance frequency of the spectrum measured at the lowest power (-74 dBm). f_n was defined as the peak frequency and, in the limit of high input power, the frequency at which the discontinuity occurs. The sign of δf serves as an indication of the polarity of the bending. A positive δf corresponds to the nonlinear spectrum bending to the higher frequency side, and a negative δf corresponds to the spectrum bending to the lower frequency side.

In Fig. 5 the normalized frequency δf of the resonance spectrum is plotted for increasing input power from -74 dBm to -54 dBm. The measurements of the spectra were made with a forward frequency sweep. The different markers correspond to various flux biases between $\Phi_{dc} = 0$ to $0.5\,\Phi_o$. At $\Phi_{dc} = 0.5\,\Phi_o$ (top plot), δf is increasingly positive; whereas, at $\Phi_{dc} = 0$ (bottom plot), δf becomes increasingly negative. Furthermore, the amount of bending $|\delta f|$ at $\Phi_{dc} = 0$ is smaller than

at $0.5\,\Phi_o$ for a given input bias, which is related to the fact that a forward frequency sweep captures the full frequency extent of the bistable region for $\Phi_{dc} = 0.5\,\Phi_o$ but not for $\Phi_{dc} = 0$. (The reverse is true if the frequency is swept backwards, as discussed in the next section.) Finally at intermediate flux biases between $0.3\,\Phi_o$ to $0.36\,\Phi_o$, δf shows an undulating behavior, corresponding to the asymmetric spectrum constantly varying its polarity. There is an initial linear dependence of δf on input power, which will be discussed in the next section.
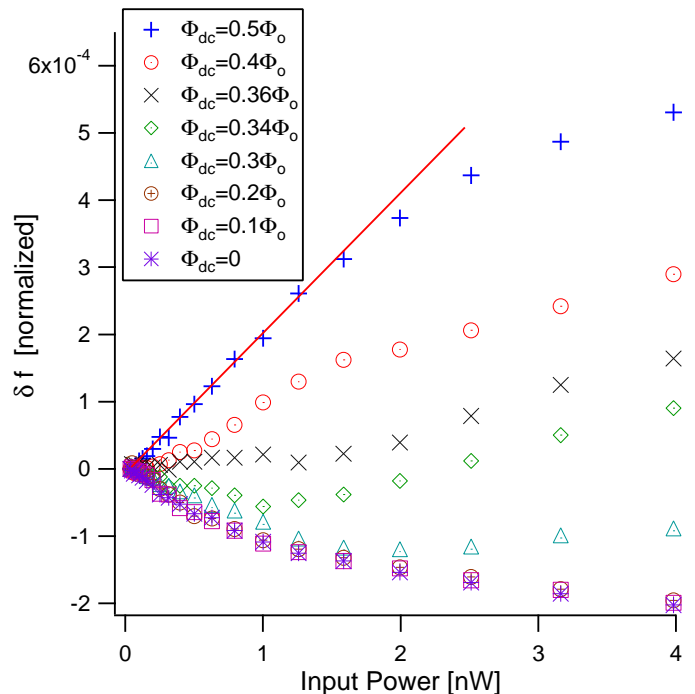

FIG. 5: (Color online) Bending δf as a function of input power from -74 dBm to -54 dBm in 1 dB steps. Measurements were made with a forward frequency sweep. The data are shown for various DC flux biases between 0 to $0.5\,\Phi_o$. The sign of δf indicates the polarity of the asymmetric spectrum. The red line corresponds to a linear fit in the low-power regime.

IV. HYSTERESIS OF THE RESONANCE SPECTRUM

For larger input drives, the resonance spectrum exhibits a discontinuity which corresponds to one of the two boundaries of the bistable region. Within the bistable region, the system settles into one of the solutions depending upon the initial conditions. For our case, the initial condition is set by the solution at the previous driving frequency, which in turn is determined by the direction of the frequency sweep. The resonant behavior of the readout circuit presented so far were obtained with a forward frequency sweep. Here, we present the hysteretic behavior of the resonance spectrum measured with both

forward and backward frequency sweeps so that the full boundary of the bistable region can be mapped.
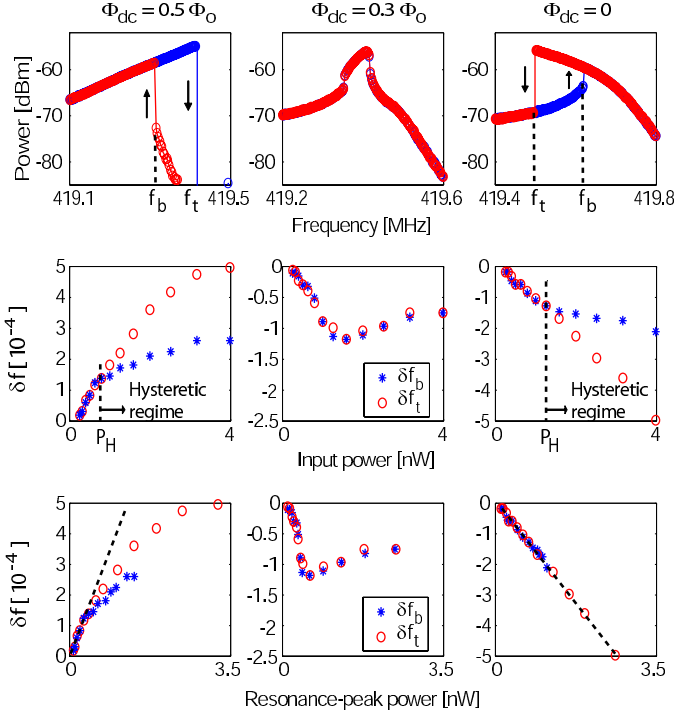

FIG. 6: (Color online) Top plots: Hysteretic resonance spectrum for flux biases at $\Phi_{dc} = 0$, $0.3\,\Phi_o$ and $0.5\,\Phi_o$. The extent of the bistable region is given by $|f_t - f_b|$. Middle plots: δf_t and δf_b as a function of input power from -66 dBm to -54 dBm in 1 dB steps. Onset of hysteretic regime occurs at P_H=-61 dBm for $\Phi_{dc} = 0.5\,\Phi_o$ and P_H=-59 dBm for $\Phi_{dc} = 0$. Bottom plots: δf_t and δf_b re-plotted as a function of resonance-peak power. The dotted line is a linear fit for low power.

The top three plots in Fig. 6 show the typical hysteretic spectrum for flux biases at $\Phi_{dc} = 0$, $0.3\,\Phi_o$ and $0.5\,\Phi_o$. The data are shown for an input power level of -54 dBm, which corresponds to a highly nonlinear regime. The direction of the frequency sweep is indicated by the arrows. For the case of $\Phi_{dc} = 0$ and $0.5\,\Phi_o$, we define the extent of the bistable region as $|f_t - f_b|$, where f_b is the frequency at which the resonance spectrum jumps from the lower to the higher stable branch, and f_t corresponds to the frequency at which the spectrum falls from the higher to the lower stable branch. At $\Phi_{dc} = 0.3\,\Phi_o$, the forward and backward traces overlapped, indicating that the bistable region associated with the two discontinuous edges were too small to be detected given the frequency resolution.

The onset of the hysteretic regime is illustrated in the middle three plots of Fig. 6, where the extent of the bistable region was characterized as a function of input power from -66 dBm to -54 dBm in 1 dB steps. First, we normalized f_t and f_b with respect to the resonance frequency f_o in the linear regime according to a definition

similar to Eqn. 7:

$$\delta f_t = \frac{f_t - f_o}{f_o} \qquad \text{and} \qquad \delta f_b = \frac{f_b - f_o}{f_o} \qquad (8)$$

δf_t and δf_b were then plotted as a function of input power. Hysteretic behavior was observed when the input bias was above a threshold P_H, which was measured to be -61 dBm for $\Phi = 0.5\,\Phi_o$, and at a higher power of -59 dBm for $\Phi = 0$.

In the bottom row of plots of Fig. 6, we have plotted δf_t and δf_b as a function of the resonance-peak power. We see that δf_t is initially a linear function of the resonance-peak power for all three fluxes shown and that it is fully linear for zero DC flux. This initial linear dependence on resonance peak power is found for many functional forms of the nonlinear term $h(\Phi, d\Phi/dt)$ [33, 34]. However, the dependence on input power varies according to the particular functional form of $h(\Phi, d\Phi/dt)$, see reference [34] for some sample cases. For example, both the Duffing equation and the pendulum model give a linear dependence on both input and resonance-peak powers in the weakly nonlinear regime [34, 35, 36]. For $h = \Phi(d\Phi/dt)^2$, δf_t depends linearly on the resonance-peak amplitude, but as the cube root of the input power [34].

V. SIMULATIONS OF NONLINEAR RESONANT BEHAVIOR BASED ON A PHENOMENOLOGICAL MODEL

In this section, we present simulations to illustrate the nonlinear resonant behavior of the readout circuit. One approach to simulate the AC-driven behavior of a circuit comprising a SQUID is to numerically solve the set of coupled differential equations governing the SQUID consistently with the rest of the circuit. However, the dynamical modeling of the resulting circuit is complex; for example, for a circuit with a SQUID shunted by a resonating capacitor has 6 dynamical variables when the mutual inductive coupling between the SQUID and the resonating loop is included [29]. Therefore, we use the phenomenological LRC circuit model of Eqn. 6 with the linear inductance replaced by a flux-dependent nonlinear inductor. This approach allows a reduction of the mathematical complexity of the problem to one dynamical variable.

Specifically, the readout SQUID is modeled by a flux-dependent nonlinear inductor $L_J(\Phi_{ext})$ given by

$$L_J(\Phi_{ext}) = \frac{L_o}{\sqrt{(1+\beta^2) + (1-\beta^2)\cos(2\pi\Phi_{ext}/\Phi_o)}} . \quad (9)$$

The functional form for the nonlinear inductor $L_J(\Phi_{ext})$ in Eqn. 9 captures the sinusoidal-like shape of the frequency response of the actual readout circuit as previously shown in Fig. 2b. This is also illustrated in Fig. 7b, where $L_J(\Phi_{ext})$ is plotted for $L_o = \sqrt{2}L_{Jo}$ (Eqn. 2), and for different values of β. It can be seen that β has an
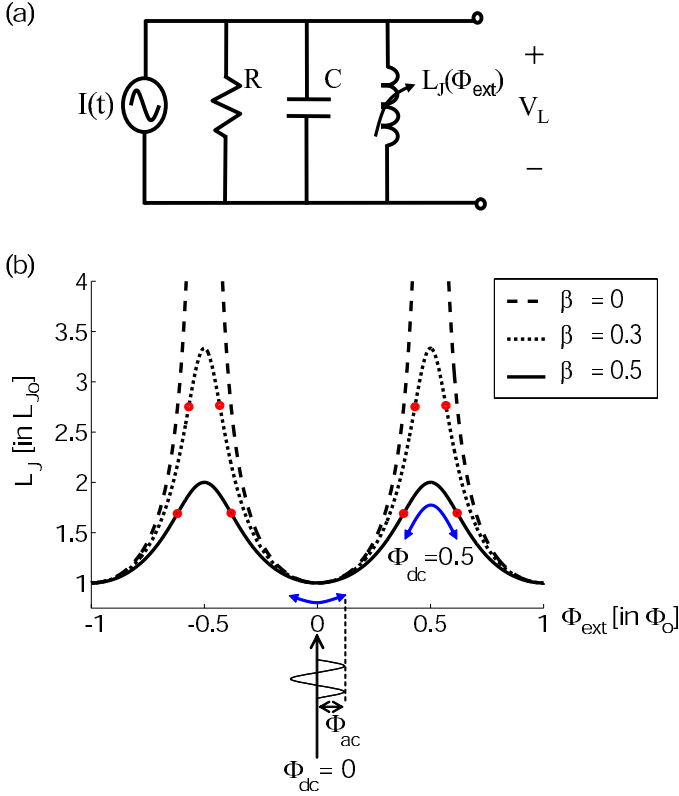
FIG. 7: (a) Circuit schematic of the phenomenological resonant model. (b) A plot of $L_J(\Phi_{ext})$ given by Eqn. 9 for different values of β. The circular markers represent the inflection points where $d^2 L_J/d\Phi^2$ is zero. The illustration shows that depending on the DC flux bias, the AC modulation of L_J due to Φ_{ac} can result in a lower ($\Phi_{dc} = 0.5\,\Phi_o$) or higher ($\Phi_{dc} = 0$) effective inductance .

effect on (a) the amount by which L_J is modulated over half a flux quantum, and (b) the position of the inflection points at which the second derivative $d^2 L_J/d\Phi^2$ is zero. One can therefore use β in Eqn. 9 as a fitting parameter such that the location of the inflection points of the frequency response ($d^2 f_o/d\Phi^2 = 0$) match the data in Fig. 2b. The functional form of the inductance was motivated by that of an asymmetric SQUID [37] since it has the needed periodicity; however, it is only the form that is used, and we are not assuming that asymmetry plays any role in the physical circuit.

We further assume that the inductor is mutually coupled to a total external flux bias as $\Phi_{ext} = \Phi_{dc} + \Phi_{ac}$, where Φ_{dc} is the DC flux bias that was applied experimentally to the SQUID, and Φ_{ac} is any oscillating flux that was mutually coupled to the SQUID. This AC-part of the flux is modeled as being proportional to the self-induced flux as $\Phi_{ac} = \alpha\Phi$ to ensure that the amount of coupled flux increases as Φ gets large near the resonance frequency of the circuit. The size of Φ_{ac} used in the simulations is around $0.1\,\Phi_o$ near the resonance frequency.

The dynamics of the phenomenological resonant circuit

is then governed by Eqn. 6 and

$$h = \frac{\Phi}{L_J(\Phi_{ext})} \tag{10}$$

For small drives ($\alpha \approx 0$), this term can be approximated by a linear inductance which depends on Φ_{dc} in a sinusoidal-like fashion. For larger values of the drive, Eqn. 10 can be expanded to be in the form of $a\,\Phi + b\,\Phi^2 + c\,\Phi^3$ when $(1 - \beta^2)/(1 + \beta^2) << 1$. Moreover, $b \sim \sin(2\pi\Phi_{dc}/\Phi_o)$ and $c \sim \cos(2\pi\Phi_{dc}/\Phi_o)$. For $\Phi_{dc} = 0$ and $\Phi_{dc} = 0.5\,\Phi_o$, then $b = 0$, and the resulting equation is of the form of a Duffing Equation with both a linear and cubic term in Φ, so that with increasing drive there will be a bending of the resonance frequency with its associated hysteresis [34] . Moreover, the sign of the cubic term is opposite for $\Phi_{dc} = 0$ and $\Phi_{dc} = 0.5\,\Phi_o$, and hence bending will be in opposite directions, as needed to qualitatively explain the data. At other values of Φ_{dc} there will be a competition between the quadratic and cubic terms.
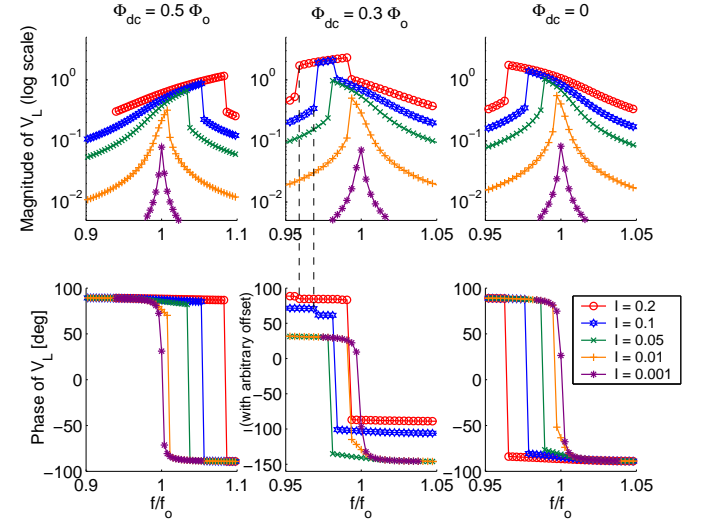

FIG. 8: (Color online) Simulated magnitude and phase spectra of V_L for increasing drive amplitude I. The results qualitatively reproduce the experimentally observed behavior in Fig. 3. V_L is plotted in reduced units of $\Phi_o/\sqrt{L_{Jo}C}$ and I in units of $2I_{co}$. The frequency axes are normalized with respect to the resonance frequency of the linear spectrum: $f_o = 1.88\,\mathrm{GHz}$ ($\Phi_{dc} = 0$), $1.59\,\mathrm{GHz}$ ($0.3\,\Phi_o$) and $1.33\,\mathrm{GHz}$ ($0.5\,\Phi_o$). The phase spectra at the highest drives I $= 0.1$ and 0.2 for $\Phi_{dc} = 0.3\,\Phi_o$ are arbitrarily shifted for display purpose.

By numerically solving Eqn. 6 for Φ at different driving frequencies ω_s, the magnitude and phase spectra of the voltage across the inductor $V_L = d\Phi/dt$ were obtained. In Fig. 8 the spectra are shown for increasing drive amplitude for $\Phi_{dc} = 0$, $0.3\,\Phi_o$ and $0.5\,\Phi_o$. V_L is plotted in reduced units of $\Phi_o/\sqrt{L_{Jo}C}$, and the drive amplitude I is in units of $2I_{co}$. The driving frequency was swept such that the lower stable branch within the bistable region

is shown for all flux biases. The simulation qualitatively resembles the experimental data presented in Fig. 3. As expected, the nonlinear spectrum has a lower resonance frequency at $\Phi_{dc} = 0$, and a higher resonance frequency at $\Phi_{dc} = 0.5\,\Phi_o$. Also, discontinuities are observed at the boundary of the bistable region for the higher biases. At $\Phi_{dc} = 0.3\,\Phi_o$, the magnitude spectra at the two highest input biases exhibit two discrete jumps, once at a lower frequency when the magnitude is increasing, and another at a higher frequency when the magnitude is decreasing. As for the phase spectra, a partial phase drop occurs at the low-frequency discontinuity, while most of the phase drop occurs at the high-frequency discontinuity.

We have also performed simulations which qualitatively reproduce the hysteresis data in Fig. 6. This was done by stepping the driving frequency in both the low-to-high and high-to-low frequency directions, and by ensuring the initial conditions used for the next frequency point were the solutions obtained for the previous frequency point. We have assumed that the square of the drive amplitude I^2 for the simulations is proportional to the input power for the experiment.

The top row of plots in Fig. 9 shows the typical simulated hysteretic behavior at various flux biases for $I/2I_{co} = 0.01$. The extent of the bistable region given by $|\delta f_b - \delta f_t|$ is the largest at $\Phi_{dc} = 0.5\,\Phi_o$ for this drive amplitude. The middle and bottom rows of plots show the dependence of δf_b and δf_t as a function of input power and resonance-peak power respectively. The trend at $\Phi_{dc} = 0.3\,\Phi_o$ shows qualitative resemblance to the experimental data. The magnitude of δf_t initially increases linearly with the power of the drive for $\Phi_{dc} = 0$ and $0.5\,\Phi_o$ similar to the data. As explained previously, this linear dependence is expected at low drives due to the nature of the nonlinearity [34, 36].

The phenomenological model presented here is meant to show the qualitative trends in the data. To be more quantitative, we have analyzed more complex circuits [29]. For example, we have considered the current-driven circuit across an asymmetric SQUID with self-inductance, and mutual inductive coupling between the SQUID loop and the resonating loop. The induced flux in the resonating loop is enhanced by the quality factor Q near the resonance frequency. The simulation gives results which qualitatively reproduce the data with reasonable numbers; however, the quantitative fitting of the data was not possible due to the uncertainty in the actual on-chip values for the capacitances and the mutual/self inductances.

VI. DISCUSSION

In this paper, we characterized the resonant behavior of the readout circuit to be utilized in a resonant scheme for measuring a PC qubit. We have identified the linear, nonlinear (bistable), and hysteretic (highly nonlinear) bias regimes of operation. Given the high quality
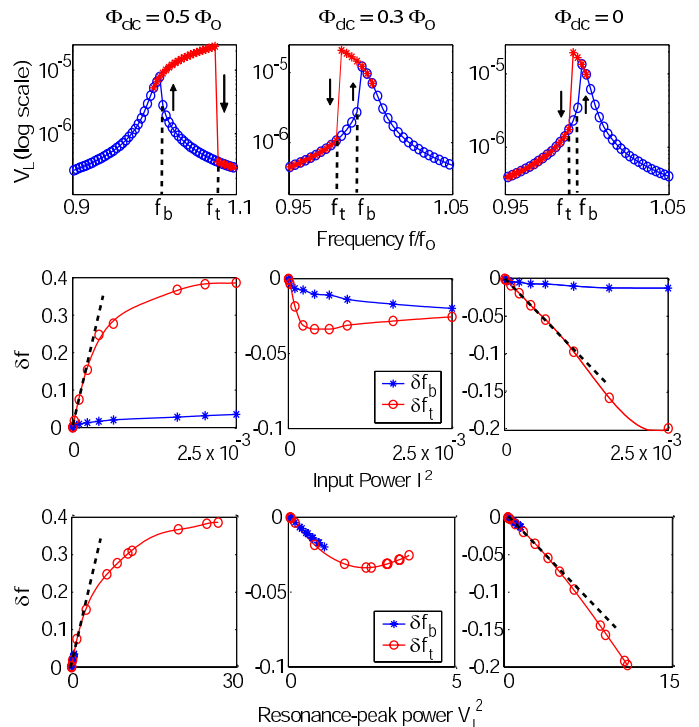

FIG. 9: (Color online) Top row: simulated hysteretic behavior at various flux bias for drive amplitude $I = 0.01$. Middle row: δf_b and δf_t as a function of the square of the drive amplitude, which is proportional to the input power. The simulations were performed for I between 0.001 to 0.05. Bottom row: δf_b and δf_t as a function of the square of the voltage response V_L, which is proportional to the resonance-peak power. V_L is in reduced units of $\Phi_o/\sqrt{L_{Jo}C}$ and I is in units of $2I_{co}$.

factor of the resonance, we observed a manifestation of the nonlinearity due to the Josephson inductance of the readout SQUID. The resonance spectrum of the readout circuit became asymmetric in the nonlinear regime, and the polarity of the asymmetry changed sign as a function of DC magnetic flux bias to the SQUID. The numerical simulations using a nonlinear inductor qualitatively reproduce the trends in the experimental data.

To perform time-resolved measurements of the qubit on a microsecond timescale, the resonant readout is to be operated at a bias frequency f_s near the resonance frequency f_o. The change in the resonance frequency due to the qubit signal is thus detected as a difference in the magnitude or phase of the output voltage at f_s.

Finally, it should be mentioned that while operating the resonant readout in the linear regime keeps the input bias low and reduces the level of decoherence on the qubit, the readout operated in the nonlinear regime has the advantage of being used as a bifurcation amplifier [24]. In particular, the bias frequency f_s can be chosen within the bistable region of the nonlinear spectrum such that the system has two stable solutions corresponding to different voltages. The probability of occupancy in

the higher/lower stable solution is sensitive to changes in the resonance frequency f_o (qubit-mediated) relative to f_s, and thus provides additional sensitivity for qubit readout over the linear approach.

VII. ACKNOWLEDGEMENTS

[1] Y. Makhlin, G. Schön, A. Shnirman, *Rev. Mod. Phys.* **73**, 357 (2001).

[2] J. Clarke, A. N. Cleland, M. H. Devoret, D. Esteve, J. H. Martinis, *Science* **239**, 992 (1988).

[3] J. R. Friedman, V. Patel, W. Chen, S. K. Tolpygo, J. E. Lukens, *Nature* **406**, 43 (2000).

[4] C. H. van der Wal, A. C. J. ter Haar, F. K. Wilhelm, R. N. Schouten, C. J. P. M. Harmans, T. P. Orlando, S. Lloyd, J. E. Mooij, *Science* **290**, 773 (2000).

[5] Y. Nakamura, Yu. A. Pashkin, and J. S. Tsai, Nature **398**, 786 (1999).

[6] I. Chiorescu, Y. Nakamura, C. J. P. M. Harmans, and J. E. Mooij, Science **299**, 1869 (2003).

[7] T. Kutsuzawa, H. Tanaka, S. Saito, H. Nakano, K. Semba, H. Takayanagi, Appl. Phys. Lett. **87**, 073501 (2005).

[8] B.L.T. Plourde, T.L. Robertson, P.A. Reichardt, T. Hime, S. Linzen, C.-E. Wu, and John Clarke, Phys. Rev. B **72**, 060506(R) (2005).

[9] Y. Yu, S. Han, X. Chu, S. Chu, and Z. Wang, Science **296**, 889 (2002).

[10] J. M. Martinis, S. Nam, J. Aumentado, and C. Urbina, Phys. Rev. Lett. **89**, 117901 (2002).

[11] D. Vion, A. Aassime, A. Cottet, P. Joyez, H. Pothier, C. Urbina, D . Esteve, and M.H. Devoret, Science **296**, 886 (2002).

[12] I. Chiorescu, P. Bertet, K. Semba, Y. Nakamura, C.J.P.M. Harmans, and J.E. Mooij, *Nature* **431**, 159 (2004).

[13] A. Wallraff, D. I. Schuster, A. Blais, L. Frunzio, R.-S. Huang, J. Majer, S. Kumar, S. M. Girvin and R. J. Schoelkopf, *Nature* **431**, 162 (2004).

[14] J. Johansson, S. Saito, T. Meno, H. Nakano, M. Ueda, K. Semba, and H. Takayanagi, *Phys. Rev. Lett.* **96**, 127006 (2006).

[15] W. D. Oliver, Y. Yu, J. C. Lee, K. K. Berggren, L. S. Levitov, T. P. Orlando, *Science* **310**, 1653 (2005).

[16] M. Sillanpää, T. Lehtinen, A. Paila, Yu. Makhlin, P. Hakonen, *Phys. Rev. Lett.* **96**, 187002 (2006).

[17] D.M. Berns, W.D. Oliver, S.O. Valenzuela, A.V. Shytov, K.K. Berggren, L.S. Levitov, T.P. Orlando, cond-mat/0606271 (*unpublished*).

[18] Yu. A. Pashkin, T. Yamamoto, O. Astafiev, Y. Nakamura, D. V. Averin, and J. S. Tsai, Nature **421**, 823 (2003).

[19] A. J. Berkley, H. Xu, R. C. Ramos, M. A. Gubrud, F. W. Strauch, P. R. Johnson, J. R. Anderson, A. J. Dragt, C. J. Lobb, and F. C. Wellstood, Science **300**, 1548 (2003).

[20] T. Yamamoto, Yu. A. Pashkin, O. Astafiev, Y. Nakamura, J. S. Tsai, Nature **425**, 941 (2003).

[21] A. Lupascu, E. F. C. Driessen, L. Roschier, C. J. P. M. Harmans, J. E. Mooij, Phys. Rev. Lett. **96**, 127003 (2006).

[22] M. Grajcar, A. Izmalkov, E. Il'ichev, Th. Wagner, N. Oukhanski, U. Hübner, T. May, I. Zhilyaev, H. E. Hoenig, Ya. S. Greenberg, V. I. Shnyrkov, D. Born, W. Krech, H.-G. Meyer, Alec Maassen van den Brink, and M. H. S. Amin, Phys. Rev. B **69**, 060501(R) (2004).

[23] A. Wallraff, D. I. Schuster, A. Blais, L. Frunzio, J. Majer, M. H. Devoret, S. M. Girvin, and R. J. Schoelkopf, Phys. Rev. Lett. **95**, 060501 (2005).

[24] I. Siddiqi, R. Vijay, M. Metcalfe, E. Boaknin, L. Frunzio, R.J. Schoelkopf, and M.H. Devoret, Phys. Rev. B **73**, 054510 (2006).

[25] B. Abdo, E. Segev, O. Shtempluck and E. Buks, Phys. Rev. B **73**, 134513 (2006).

[26] C. C. Chin, D. E. Oates, G. Dresselhaus, and M. S. Dresselhaus, Phys. Rev. B **45**, 4788 (1992).

[27] J. E. Mooij, T. P. Orlando, L. Levitov, L. Tian, C. van der Wal, and S. Lloyd, Science **285**, 1036 (1999).

[28] T. P. Orlando, J.E. Mooij, L. Tian, C.H. van der Wal, L. Levitov, S. Lloyd, and J.J. Mazo, Phys. Rev. B **60**, 15398 (1999).

[29] J. C. Lee, Ph.D. thesis, MIT, 2006.

[30] C. Bowick, *RF Circuit Design* (Newnes Press, 1982).

[31] K. Berggren, E. Macedo, D. Feld, and J. Sage, IEEE Trans. Applied Supercond. **9**, 3271 (1999).

[32] J. C. Lee, W. D. Oliver, T. P. Orlando, K. K. Berggren, IEEE Trans. Applied Supercond. **15**, 841 (2005).

[33] Steven H. Strogatz, *Nonlinear Dynamics and Chaos*, (Addison-Wesley, 1994).

[34] A. H. Nayfeh, and D. T. Mook, *Nonlinear Oscillations*, (John Wiley & sons, 1979).

[35] F. Kouril, and K. Vrba, *Non-linear and parametric circuits, Principles, theory and applications*, (John Wiley & sons, 1988).

[36] L. D. Landau, and E. M. Lifshitz, *Mechanics*, (Pergamon Press Ltd., 1960).

[37] A. Barone, and G. Paterno, *Physics and applications of the Josephson effect*, (John Wiley & sons, 1982).

[38] T. Holst, J. Bindslev Hansen, Physica B **165-166**, 1649 (1990).